Numerical Simulation of the Airflow Over Barbados

YTZHAQ MAHRER AND ROGER A. PIELKE[1]

Department of Environmental Sciences, University of Virginia, Charlottesville 22903

(Manuscript received 4 March 1976, in revised form 1 August 1976)

ABSTRACT

A hydrostatic three-dimensional primitive equation model, which includes topography and detailed boundary layer parameterization, has been developed to simulate the lower tropospheric flow overv Barbados on synoptically undisturbed days. Observations indicate that on such days island precipitation shows a distinct nighttime maximum. Using observed data for the initial conditions, the model is first integrated to a steady-state solution, whereupon a diurnal temperature wave is imposed on the island surface. Three experiments are run: 1) with a realistic representation of the terrain and shape of Barbados, 2) with no terrain but a realistic shape, and 3) with a cross section of Barbados where three-dimensional asymmetries of terrain and coastline are ignored. Results indicate that topography is an important factor in the modification of low-level flow over Barbados, only in a three-dimensional representation does upward motion develop downwind of the west coast, as observed, and the nocturnal rainfall maximum may be attributed to a moister nighttime low-level environment as compared to the day. Additional meteorological observations are needed to verify certain aspects of the model predictions.

1. Introduction

Observational studies over Barbados by Garstang (1967) and DeSouza (1972) indicate that on synoptically undisturbed days, island precipitation shows a distinct nighttime maximum. DeSouza (1972) argues that such a nocturnal maximum is characterized by low-level daytime divergence and nighttime convergence. Garstang (1967) attempts to explain the apparent daytime acceleration over the island in terms of vertical eddy transport processes, while Estoque and Bhumralkar (1969) contend, from a two-dimensional steady-state numerical model, that horizontal advective processes by a basic flow are much more important than the eddy transport process. Lee (1973) included topographic effects in his two-dimensional model of air flow over Barbados and suggested that topography plays a dominant role in the modification of the low-level flow over the island. A recent work by Emmitt (1975) maintains that the sign and magnitude of the vertical shear of the horizontal wind helps to explain day to day variation in the precipitation and velocity fields over Barbados.

The three-dimensional University of Virginia mesoscale model[2] has been adapted to study the air flow over Barbados. As in our previous paper (Mahrer and Pielke, 1975) the basic equations are transformed into a terrain-following coordinate system (x,y,z^*,t) by the transformation

$$z^*=\bar{s}\frac{z-z_G(x,y)}{s(x,y,t)-z_G(x,y)},$$

where $\bar{s}$ is the initial height of the top of the model, s is the material surface top of the model (initially $s=\bar{s}$) and $z_G(x,y)$ is the ground elevation.

A diurnal temperature wave is imposed over the island surface after a steady-state solution is achieved. Three versions of the model are discussed:

1) With topography
2) Without topography
3) Two-dimensional forcing with topography.

2. Basic equations

Using the terrain-following coordinate system, the three-dimensional equations of motion, heat, moisture and continuity for hydrostatic motion are as follows (symbols defined in the Appendix):

$$\frac{du}{dt}=fv-fV_g-\theta_v\frac{\partial\pi}{\partial x}+g\frac{z^*-\bar{s}}{\bar{s}}\frac{\partial z_G}{\partial x}-g\frac{z^*}{\bar{s}}\frac{\partial s}{\partial x}+\left(\frac{\bar{s}}{s-z_G}\right)^2\times\frac{\partial}{\partial z^*}\left(K_z^m\frac{\partial u}{\partial z^*}\right)+\frac{\partial}{\partial x}\left(K_H\frac{\partial u}{\partial x}\right)+\frac{\partial}{\partial y}\left(K_H\frac{\partial u}{\partial y}\right), \quad (1)$$

[1] Also affiliated with the Center for Advanced Studies, University of Virginia.

[2] The University of Virginia model is an improved version of the model discussed by Pielke (1974). Some of the improvements are discussed in Pielke and Mahrer (1975) and Mahrer and Pielke (1975).

$$\frac{dv}{dt}=-fu+fU_g-\theta_v\frac{\partial\pi}{\partial y}+g\frac{z^*-\bar{s}}{\bar{s}}\frac{\partial z_G}{\partial y}-g\frac{z^*}{\bar{s}}\frac{\partial s}{\partial y}+\left(\frac{\bar{s}}{s-z_G}\right)^2 \times\frac{\partial}{\partial z^*}\left(K_z^m\frac{\partial v}{\partial z^*}\right)+\frac{\partial}{\partial x}\left(K_H\frac{\partial v}{\partial x}\right)+\frac{\partial}{\partial y}\left(K_H\frac{\partial v}{\partial y}\right), \quad (2)$$

$$\frac{d\theta_v}{dt}=\left(\frac{\bar{s}}{s-z_G}\right)^2\frac{\partial}{\partial z^*}\left(K_z^{\theta_v}\frac{\partial\theta_v}{\partial z^*}\right)+\frac{\partial}{\partial x}\left(K_H\frac{\partial\theta_v}{\partial x}\right)+\frac{\partial}{\partial y}\left(K_H\frac{\partial\theta_v}{\partial y}\right), \quad (3)$$

$$\frac{dq}{dt}=\left(\frac{\bar{s}}{s-z_G}\right)^2\frac{\partial}{\partial z^*}\left(K_z^q\frac{\partial q}{\partial z^*}\right)+\frac{\partial}{\partial x}\left(K_H\frac{\partial q}{\partial x}\right)+\frac{\partial}{\partial y}\left(K_H\frac{\partial q}{\partial y}\right), \quad (4)$$

$$\frac{\partial u}{\partial x}+\frac{\partial v}{\partial y}+\frac{\partial w^*}{\partial z^*}-\frac{1}{s-z_G}\left(u\frac{\partial z_G}{\partial x}+v\frac{\partial z_G}{\partial y}\right)+\frac{1}{s-z_G}\left(\frac{\partial s}{\partial t}+u\frac{\partial s}{\partial x}+v\frac{\partial s}{\partial y}\right)=0, \quad (5)$$

$$\frac{\partial\pi}{\partial z^*}=-\frac{s-z_G}{\bar{s}}g/\theta_v, \quad (6)$$

where

$$\pi=c_p\left(\frac{p}{p_{00}}\right)^{R/c_p},$$

$$w^*=\frac{\bar{s}}{s-z_G}w-\frac{z^*}{s-z_G}\left(\frac{\partial s}{\partial t}+u\frac{\partial s}{\partial x}+v\frac{\partial s}{\partial y}\right)+\frac{z^*-\bar{s}}{s-z_G}\left(u\frac{\partial z_G}{\partial x}+v\frac{\partial z_G}{\partial y}\right),$$

$$\frac{d}{dt}=\frac{\partial}{\partial t}+u\frac{\partial}{\partial x}+v\frac{\partial}{\partial y}+w^*\frac{\partial}{\partial z^*}.$$

In order to solve the above set of equations, an additional equation for the height of the material surface s must be obtained. By integrating the continuity equation (5) from the surface $z^*=0$ to the top $z^*=\bar{s}$, and assuming that w^* vanishes at both boundaries we obtain

$$\frac{\partial s}{\partial t}=-\frac{1}{\bar{s}}\int_0^{\bar{s}}\left\{\frac{\partial}{\partial x}[u(s-z_G)]+\frac{\partial}{\partial y}[v(s-z_G)]\right\}dz^*. \quad (7)$$

3. Boundary layer formulation

The vertical exchange coefficients in the surface layer are given by

$$K_z^m(z^*)=k_0u_*z^*/\phi_m(\xi) \quad (8)$$

$$K_z^{\theta_v}(z^*)=k_0u_*z^*/\phi_{\theta_v}(\xi). \quad (9)$$

The nondimensional stability length ξ is defined as $\xi=z^*/L$, where

$$L=\frac{\theta_vU_*^2}{k_0g\theta_*},$$

$$U_*=k_0(U^2+V^2)^{\frac{1}{2}}/[\ln(z/z_0)-\psi_1],$$

$$\theta_*=k_0[\theta_v-\theta_v(z_0)]/\{0.74[\ln(z/z_0)-\psi_2]\}.$$

The variables ψ_1 and ψ_2 are functions of stability and are given in Pielke and Mahrer [1975, p. 2300, Eqs. (27) and (28)], except that ψ_2 should read

$$\psi_2=\begin{cases}2\ln[(1+0.74\phi_H^{-1})/2], & \xi\leqslant 0\\ -6.35\xi, & \xi>0.\end{cases}$$

This error resulted from an apparent typographical mistake in Businger (1973, p. 77). A rerun of the day 33 Wangara simulations showed only insignificant changes so that the conclusions discussed in that paper are unaffected.

Over the land surface a roughness length of $z_0=4$ cm is used, while over water z_0 is a function of the surface stress and is defined according to Clarke (1970) as

$$z_0=0.032u_*^2/g$$

with the condition that

$$z_0\geqslant 0.0015 \text{ cm}.$$

The functional form of the exchange coefficient above the surface layer, suggested by O'Brien (1970), is given by

$$K_z(z^*)=\begin{cases}K_z|_{z_i}+(z_i-z^*)^2/(z_i-h)^2\left\{K_z|_h-K_z|_{z_i}+(z^*-h)\left[\frac{\partial}{\partial z^*}K_z\Big|_h+2(K_z|_h-K_z|_{z_i})\div(z_i-h)\right]\right\}, & z_i\geqslant z^*\geqslant h\\ K_z|_{z_i}, & z^*>z_i\\ (z^*/h)K_z|_h, & z^*<h,\end{cases}$$

where $K_z(z^*)$ refers to $K_z^m(z^*)$, $K_z^{\theta_v}(z^*)$ and $K_z^q(z^*)$, and $K_z|_{z_i}\approx 1$ cm^2 s^{-1}. The variable $K_z|_h$ is the exchange coefficient at the top of the surface layer h, which is defined as

$$h=z_i/25.$$

The values of the vertical exchange coefficients of momentum, heat and moisture at the island boundaries, weighted in proportion to the area of land and water around each grid point, are determined from

$$K_z=(1-A)K_z|_{\text{water}}+AK_z|_{\text{land}}, \quad 0\leqslant A\leqslant 1.$$

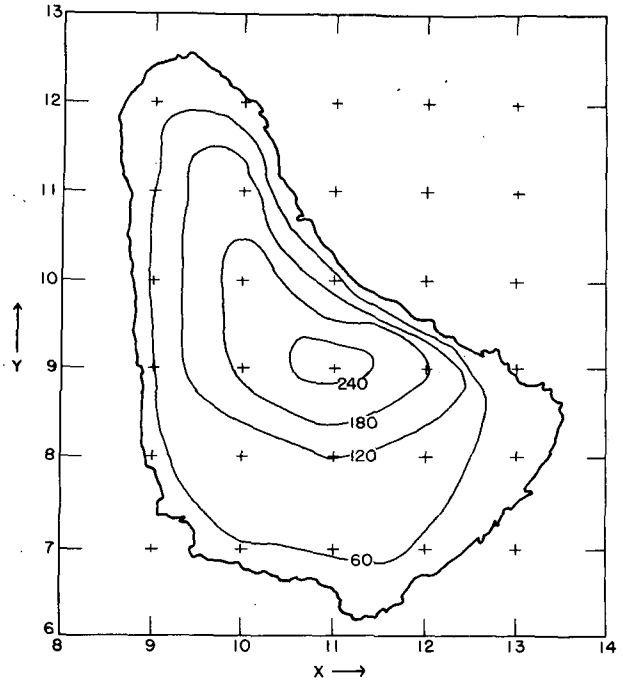

FIG. 1. Smoothed topographic map of Barbados and the outline of model grid (the grid interval is 5 km; contours in m).

The grid and map of Barbados used to determine the weights are given in Fig. 1.

The depth of the planetary boundary layer z_i is predicted by a prognostic equation based on Deardorff's (1974) work. According to Deardorff's technique, z_i grows as a function of surface heat and momentum fluxes, mesoscale and synoptic vertical motion and the overlying thermodynamic stability. In terms of our model the prognostic equation for z_i is given as

$$\frac{dz_i}{\partial t}=\frac{1.8(W_*^3+1.1u_*^3-3.3u_*^2fz_i)}{g\dfrac{z_i^2}{\theta_{vs}}\dfrac{\partial\theta_v^+}{\partial z^*}+9W_*^2+7.2u_*^2},$$

where the value of W_* is given as

$$W_*=\begin{cases}[(-g/\theta_{vs})u_*\theta_{v*}z_i]^{\frac{1}{3}}, & \theta_{v*}\leqslant 0\\ 0, & \theta_{v*}\geqslant 0.\end{cases}$$

For more details regarding the parameterization of the boundary layer, see Pielke (1974) and Pielke and Mahrer (1975).

4. Initial and boundary condition

The initial conditions for $t\leqslant 0$ are

$$p(z=z^*=0)=1013 \text{ mb}$$
$$T(z=z^*=0)=28^\circ\text{C}$$
$$U_g=-10 \text{ m s}^{-1};\quad V_g=0$$
$$q(z=z^*=0)=18 \text{ g kg}^{-1}.$$

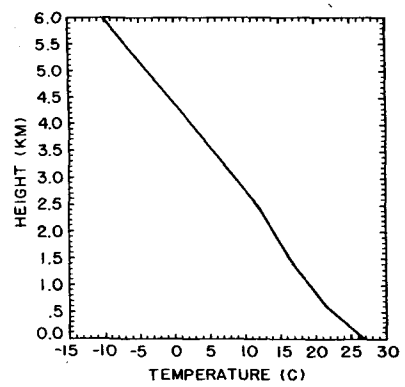

FIG. 2. Mean vertical temperature distribution for July and August 1968 (from DeSouza, 1972).

Figs. 2 and 3 show the vertical distribution of temperature and specific humidity at 0600 LST based on mean radiosonde observations during July and August 1968 (DeSouza, 1972). The values used for U_g and V_g were mean observed values for July and August, 1968 (DeSouza, 1972, Figs. 7 and 8). Over the flat surface at the initial time, before topography is introduced, the shear stress, the Coriolis and the pressure gradient forces are assumed to be in balance as expressed by

$$\frac{\partial}{\partial z}\left(K_z^m\frac{\partial u}{\partial z}\right)+f(V-V_g)=0, \tag{10}$$

$$\frac{\partial}{\partial z}\left(K_z^m\frac{\partial v}{\partial z}\right)+f(U_g-U)=0. \tag{11}$$

The initial wind profile in the planetary boundary layer is calculated from (10) and (11) using a modified version (suggested by John D. Reid, Colorado State University) of the iterative method discussed by Pielke (1974), where the time-dependent solution is integrated for six inertial periods.

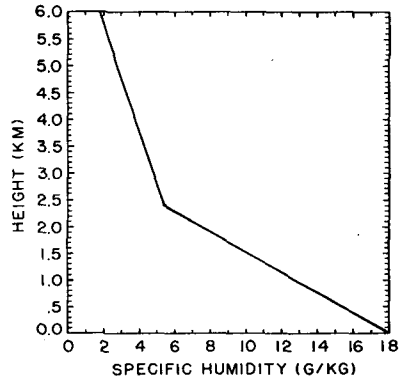

FIG. 3. Mean vertical specific humidity distribution from July and August 1968 (from DeSouza, 1972).

The boundary conditions are as follows:

(i) At $z^*=0$:

$$u=v=w^*=0$$

$q=$ constant

$\theta=28°$C over water

$$\theta=28+a_0+\sum_{m=1}^{4}\left(a_m\cos\frac{2\pi m t_D}{24}+b_m\sin\frac{2\pi m t_D}{24}\right),$$

over land at level z_0, where t_D is time in hours with $t_D=0$ at midnight, and

$$a_0=\ 2.85$$
$$a_1=-5.28 \qquad b_1=-0.92$$
$$a_2=\ 1.85 \qquad b_2=\ 0.30$$
$$a_3=\ 0.22 \qquad b_3=-0.35$$
$$a_4=-0.22 \qquad b_4=\ 0.18.$$

The above form for the diurnal temperature wave at the land surface was derived by Holley (1972) from radiometer data collected over Barbados in 1969 during the BOMEX experiment. The functional form of θ is shown in Fig. 4.

(ii) At $z^*=\bar{s}=6$ km:

$$U=U_g,\quad V=V_g,\quad w^*=0$$
$$\pi=\pi(\bar{s})-g(s-\bar{s})/\theta_v(s)$$

$\theta_v(s)=$ constant (assumption of adiabatic motion of s).

(iii) At the lateral boundaries:

$$w^*=\begin{cases}\dfrac{\partial s}{\partial t}=\dfrac{\partial}{\partial x}(\theta_v,q,\pi,z_i)=0\\[2ex]\dfrac{\partial s}{\partial t}=\dfrac{\partial}{\partial y}(\theta_v,q,\pi,z_i)=0\end{cases}$$

$\dfrac{\partial}{\partial x}(u,v)=\dfrac{\partial}{\partial y}(u,v)=0$ at the outflow boundaries

$u=$ constant, $v=$ constant at the inflow boundaries.

5. Numerical aspects

As in our previous study (1975), we followed Deaven's (1974) procedure of "diastrophism," that is, the topography is allowed to grow during the first 30 min from an initial horizontal surface up to its maximum height. Deaven's method is applied in order to avoid numerical integration problems arising from the initial accelerations. After the island has reached its maximum height, an additional 3.5 h of integration were required to achieve a steady-state solution. The existence of a steady-state solution was checked by comparing the various fields (u,v,θ,w) every hour. For example, it was found that the maximum change in the vertical velocity field during the last hour was less than 5%, with even smaller changes in the u, v and θ fields.

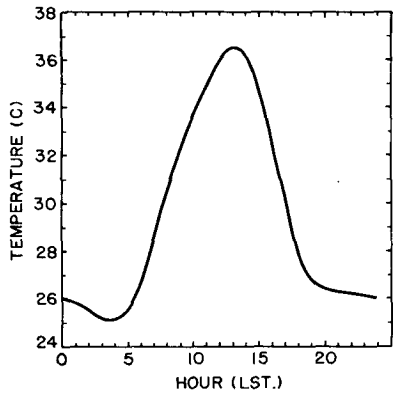

FIG. 4. Island surface temperature variation with time (from DeSouza, 1972).

A full description of the numerical procedure except for the vertical eddy transport terms is given in Pielke (1974). The vertical eddy transport terms were evaluated by an implicit difference scheme; see Mahrer and Pielke (1975). A 21×18 horizontal grid mesh with a grid interval of 5 km is used, except near the lateral boundaries where the horizontal grid interval is increased linearly to 20 km. The horizontal grid intervals are given by

$$\Delta x(i)=\begin{cases}(20-5(i-1))\ \text{[km]}, & 1\leqslant i\leqslant 4\\ 5\ \text{km} & 5\leqslant i\leqslant 17\\ (5+5(i-18))\ \text{[km]}, & 18\leqslant i\leqslant 21,\end{cases}$$

$$\Delta y(j)=\begin{cases}(20-5(j-1))\ \text{[km]}, & 1\leqslant j\leqslant 4\\ 5\ \text{km} & 5\leqslant j\leqslant 14\\ (5+5(j-15))\ \text{[km]}, & 15\leqslant j\leqslant 18.\end{cases}$$

In the vertical the atmosphere was divided into 12 levels with heights of 0, 50, 100, 300, 600, 1500, 2100, 3000, 4000, 5000 and 6000 m, where u, v, p and w are computed. θ_v and q are computed at intermediate heights. The form of the horizontal exchange coefficient in the prognostic equations (1), (2), (3) and (4) is given by

$$K_h=\alpha(\Delta x)(\Delta y)\left[\left(\frac{\partial v}{\partial x}\right)^2+\left(\frac{\partial u}{\partial y}\right)^2+0.5\left(\frac{\partial u}{\partial x}+\frac{\partial v}{\partial y}\right)^2\right]^{\frac{1}{2}}$$

where α is a numerical constant. In the present study we used $\alpha=0.36$.

6. Results

Starting at 1900 LST (after a steady-state solution is achieved) the model is integrated for the three following cases for 29 h until midnight of the second day.

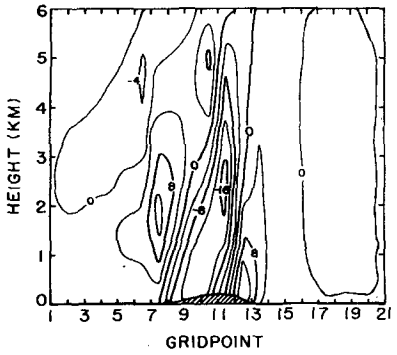

FIG. 5. The vertical velocity field in and along the widest east–west cross section of the island at 1900 LST for the real island experiment (contour interval is 4 cm s^{-1}).

a. Real island

In this experiment we will examine the effect of the surface heating (and cooling) in a three-dimensional model, including smoothed terrain approximated from a topographic map of Barbados (Fig. 1).

1) VERTICAL VELOCITIES

Perhaps the most striking features of this experiment are the diurnal changes in the vertical velocity fields off the west coast. Figs. 5–7 show the vertical velocity fields along the widest east–west cross section of the island ($j=8\frac{1}{2}$) at 1900 LST (initial time), 1300 LST and 2400 LST (the last hour of the integration), respectively. At the initial time (Fig. 5), the vertical velocity field has an upward component on the east slope due to upslope motion with a maximum value of 16 cm s^{-1}, a wide downward cell above the center and west slope attaining a maximum speed of -16 cm s^{-1} and a second upward cell off the west coast at higher elevation, with a maximum value of 13 cm s^{-1}. It should be noticed that a similar spatial vertical motion distribution was observed previously in numerical experiments of air flow over mountains by Deaven (1974) and Mahrer and Pielke (1975). At 1300 LST (Fig. 6), about the time of maximum surface heating, strong upward velocities have developed off the west coast at low

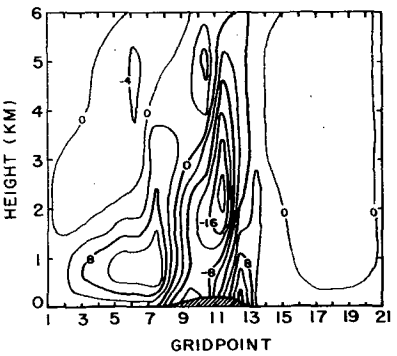

FIG. 6. As in Fig. 5 except for 1300 LST.

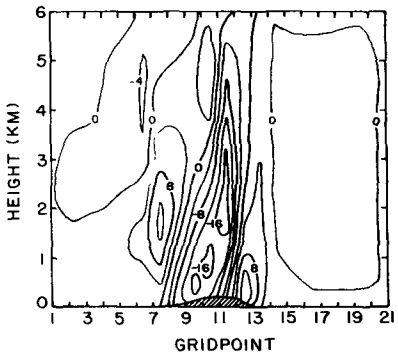

FIG. 7. As in Fig. 5 except for 2300 LST.

elevation with a maximum value of 16 cm s^{-1}, while the downward motion above the center of the island has intensified to -23 cm s^{-1}. Almost no changes are observed in the upward velocities along the east coast. At 2400 LST (Fig. 7) the upward velocities off the west coast have almost returned to their initial state (Fig. 5). Above the center of the island the downward velocities have decreased to -16 cm s^{-1}. The vertical velocity field described above agrees favorably with the constant density balloon trajectories (Fig. 8) discussed by DeSouza (1972) which sink over the center and the western part of the island, and rise again at the west coast during the day. The nighttime trajectories show slight rising inland from the east coast and sinking further inland over most of the island, with an increase in the rate of sinking near the west coast.

Figs. 9 and 10 show a horizontal section at $z^*=1$ km for 1300 LST and 2400 LST, respectively. At both times, downward motion occurs over most of the island with the largest values over the north part due to the steeper topography. Rising motion is observed over the east coast and off the west coast. The strongest upward motions during the day are west of the center of the island. We will discuss this result in the next section.

The temporal variation of the vertical velocity field above the island as described above disagrees with DeSouza's (1972) idealized fields which show daytime

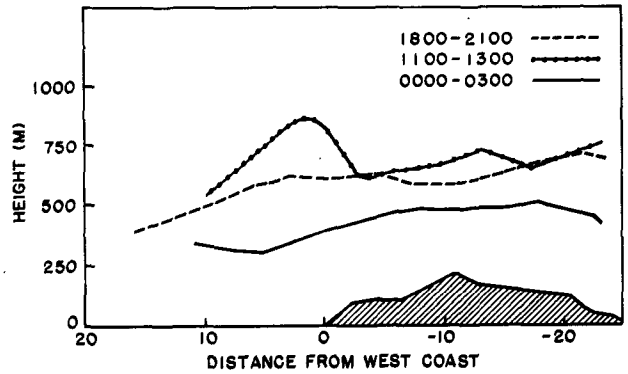

FIG. 8. Mean vertical trajectories of constant density balloons in 1968 versus horizontal distance from the west coast (from DeSouza 1972).

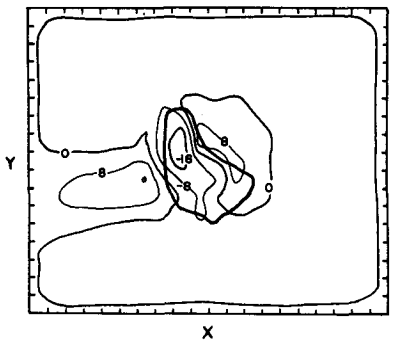

FIG. 9. The vertical velocity field at $z^*=1$ km at 1300 LST for the real island experiment (contour interval 8 cm s^{-1}).

divergence and nighttime convergence. DeSouza neglected the effect of the slope of the terrain in his divergence calculation which is important especially near the surface. With a strong easterly wind (10 m s^{-1}) the terrain effect dominates the other terms of the divergence equation. For the purpose of a first estimate let us take $v=0$, $\partial u/\partial z=10$ m s^{-1} (100 m)$^{-1}$, and $\partial z_G/\partial x=\pm 100$ m (5 km)$^{-1}$ so that the terrain term immediately above the surface is of the order of $\pm 2\times 10^{-3}$ s^{-1}, which is about one order of magnitude higher than the values calculated by DeSouza.

2) HORIZONTAL VELOCITIES

Fig. 11 shows the hourly output of the wind speed $[(u^2+v^2)^{\frac{1}{2}}]$ at a height of 8 m above the surface at three locations along the widest cross section ($j=8\frac{1}{2}$) (along the east coast, at the center and along the west coast). The velocities at 8 m are calculated from the equation

$$V=\frac{u^*}{k_0}\left(\ln\frac{z}{z_0}-\psi_1(\xi)\right),$$

where ψ_1 is the stability dependent velocity profile function (see Pielke and Mahrer, 1975). The results show a marked daytime maximum at about 1400 LST over the center of the island and along the west coast, with almost no time variations at the east coast in agreement with the observational studies by Garstang (1967) and DeSouza (1972), who observed daytime

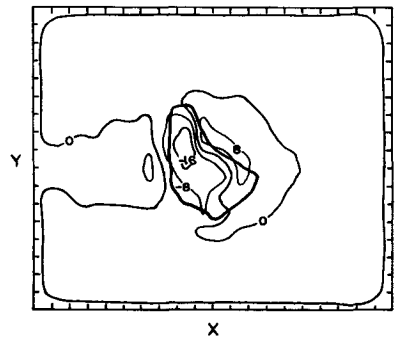

FIG. 10. As in Fig. 9 except for 2400 LST.

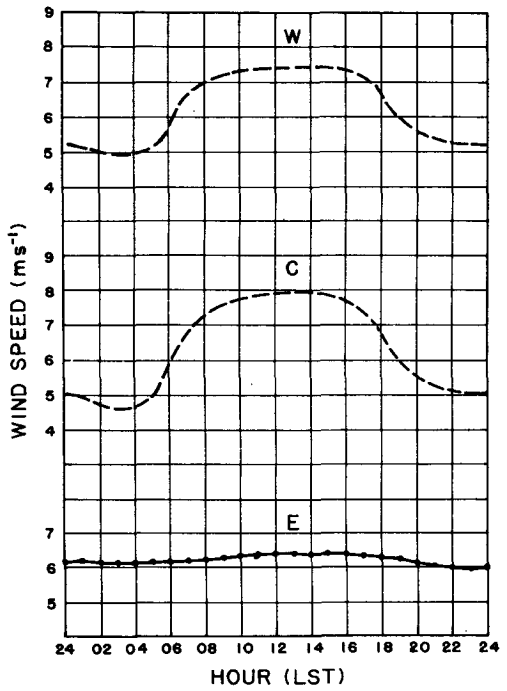

FIG. 11. The hourly output of the horizontal wind speed at a height of 8 m above the surface at three locations along the widest east–west cross section (at the east coast, at the center and at the west coast).

acceleration over the island, but none at the east coast. Vertical velocity fields calculated from those horizontal velocity distributions, neglecting topography influences (as done by DeSouza, 1972) will result in downward motion at the east coast and upward motion over and downwind of the west coast during daytime, while the opposite will be true for nighttime. Such idealized fields were presented by DeSouza (1972, Fig. 33), and were predicted in our flat island experiment (see Section 6b).

Figs. 12 and 13 show two horizontal cross sections of the horizontal wind field at 8 m above the surface corresponding to the observation level during the 1968 Barbados program. At 2400 LST (Fig. 12) the winds have decelerated over the island at that level because

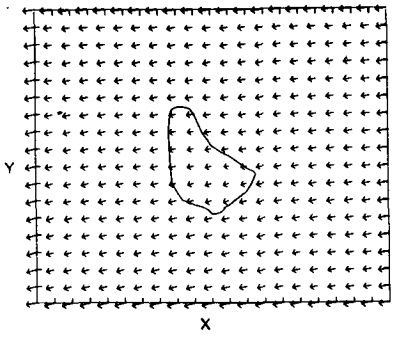

FIG. 12. The horizontal wind at $z^*=50$ m at 1900 LST for the real island experiment (the length of 1 grid interval corresponds to 10 m s^{-1}).

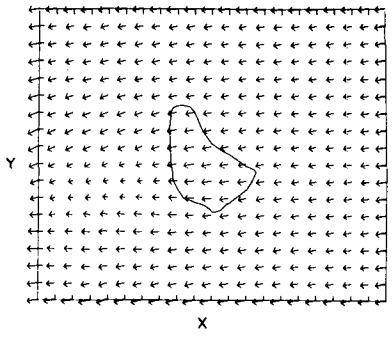

FIG. 13. As in Fig. 12 except for 1300 LST.

the surface layer is stably stratified, while at 1300 LST (Fig. 13) the winds accelerate over the island with the strongest wind speed occurring over the western part of the island. This acceleration is due to the offshore location of the heated island pressure minimum (see Fig. 16) and to some extent, because the surface layer becomes more unstably stratified westward across the island. The daily variation of the 8 m winds immediately inland from the east coast (Figs. 12 and 13) has been observed by Aspliden (personal communication) along the southeast coast. The convergence in wind direction downwind of the west coast is due to the advection downstream of the positive temperature anomaly produced by the heated island. This creates a pressure minimum in that area and the resultant wind direction change produces the upward motion mentioned before.

The vertical profile of the east–west wind component at the center of the island ($i=11$, $j=8\frac{1}{2}$) at the initial time (after a steady state was achieved) is shown in Fig. 14. A maximum and a minimum in wind velocity produced by topography are observed at about 1.2 and 4 km, respectively. The corresponding vertical

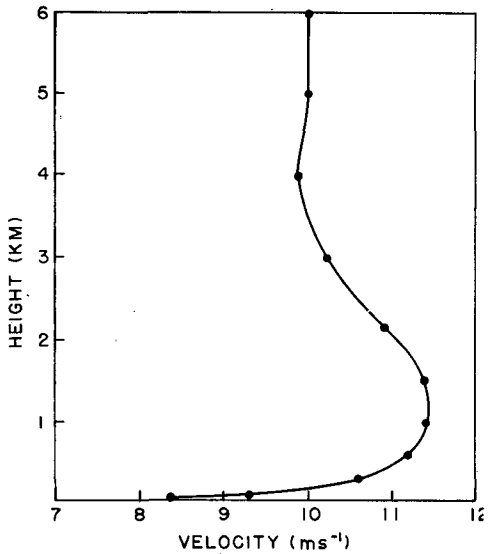

FIG. 14. Vertical profile of the east–west wind velocity component at the center of the island.

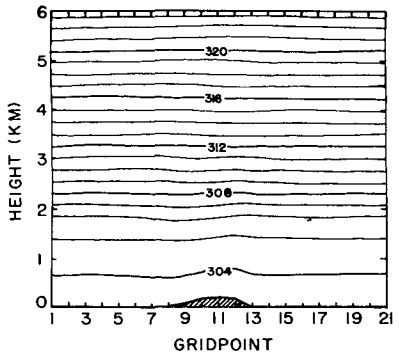

FIG. 15. Potential temperature field along the widest east–west cross section at 1900 LST for the real island experiment.

wavelength is 5.6 km, which is in agreement with the theoretical vertical wavelength calculated from the equation $L=2\pi/K_c$, where

$$K_c^2=\frac{g\dfrac{\partial\theta}{\partial z}}{\bar{\theta}U^2}, \tag{12}$$

(see Mahrer and Pielke, 1975). With $\partial\theta/\partial z=0.4\text{C}^\circ$ $(100\text{ m})^{-1}$ and $U=10\text{ m s}^{-1}$, (12) results in $L=5.4$ km. A mean vertical wind profile of this shape is observed over Barbados (Emmitt, personal communication).

3) POTENTIAL TEMPERATURE

A vertical cross section at $j=8\frac{1}{2}$ of the potential temperature field at 1900 LST is shown in Fig. 15. The isentropic surfaces near the ground follow the shape of the topography, with a temperature minimum on the windward side produced by rising motion, and a maximum on the lee side produced by sinking. Note that, although of small amplitude, both the minimum and the maximum in potential temperature tilt-up stream with height, as observed (Lilly and Kennedy, 1973) and as predicted (Hovermale, 1965; Deaven, 1974; Mahrer and Pielke, 1975) in air flow over hilly or mountainous terrain. A cross section of potential tem-

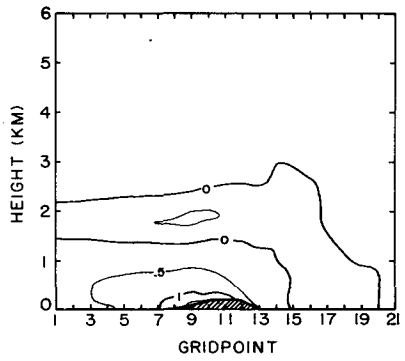

FIG. 16. Potential temperature perturbation field along the widest east–west cross section at 1300 LST for the real island experiment.

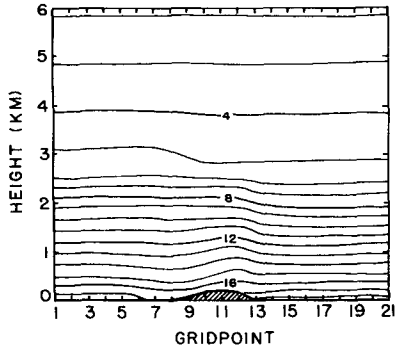

FIG. 17. Specific humidity field along the widest east–west cross section at 1300 LST for the real island experiment.

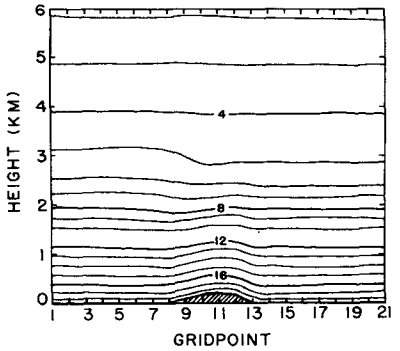

FIG. 18. As in Fig. 17 except for 2400 LST.

perature perturbation at the time of maximum surface temperature (1300 LST) is shown in Fig. 16, where, due to advection, a downwind plums is developed with an approximate depth of 1 km with a perturbation from the initial 1900 LST value of over 0.5°C extending well downstream from the west coast. At night (not shown), as cooling takes place the temperatures return almost to their initial state, resulting in a featureless perturbation field. DeSouza's (1972, Fig. 29) observations show similar day and night fields.

4) SPECIFIC HUMIDITY

Figs. 17 and 18 show isopleths of the specific humidity along the $j=8.5$ cross section at 1300 and 2400 LST, respectively. A marked daytime drying occurs over the western slopes and downwind of the island at low elevation. A maximum departure of 1 g kg^{-1} from the east coast value is observed near the surface. At higher elevations (above 1 km) the results show an excess in moisture of about 0.5 g kg^{-1} downwind of the island. At night the isopleths of specific humidity follow the shape of the mountain with only a slight drying (less than 0.2 g kg^{-1}) at a height of about 600 m over and off the west coast. For the nighttime our results disagree with DeSouza's (1972, Figs. 33 and 34,) mean observations which show an almost uniform deficit in specific humidity over the western slopes and downwind of the island during both the day and the night. However, DeSouza states that "the humidity was highly variable along the flight track with a systematic drying out west of the island *particularly noticeable during the daytime.*" DeSouza also mentions that "unlike the temperature, no particular flight leg is likely to have dew-point traces that closely resemble the overall mean." Because of the high variation in dewpoint between flights, it is difficult to determine the validity of the model results for the specific humidity from the observational data. This points out the need for further detailed observations of the air flow over Barbados.

Fig. 19 shows vertical profiles of the saturation equivalent potential temperature (θ_{es}) and equivalent potential temperature (θ_e) at 1300 and 2400 LST for the east coast, center of the island and the west coast. Fig. 20 shows the differences ($\theta_{es}-\theta_e$) which are a measure of the moistness of the atmosphere. It can be seen that there is a trend toward a cooler and moisture, nighttime, low-level atmosphere as we move inland. Betts (1974) used rawinsonde soundings taken at Carrzal, Venezuela (9°22'N, 66°55'W) to show that, from dry to disturbed days, there is a uniform trend toward a cooler, moister atmosphere. Based on Betts' observations and our results, we suggest an alternative explanation to the nighttime maximum rainfall; that

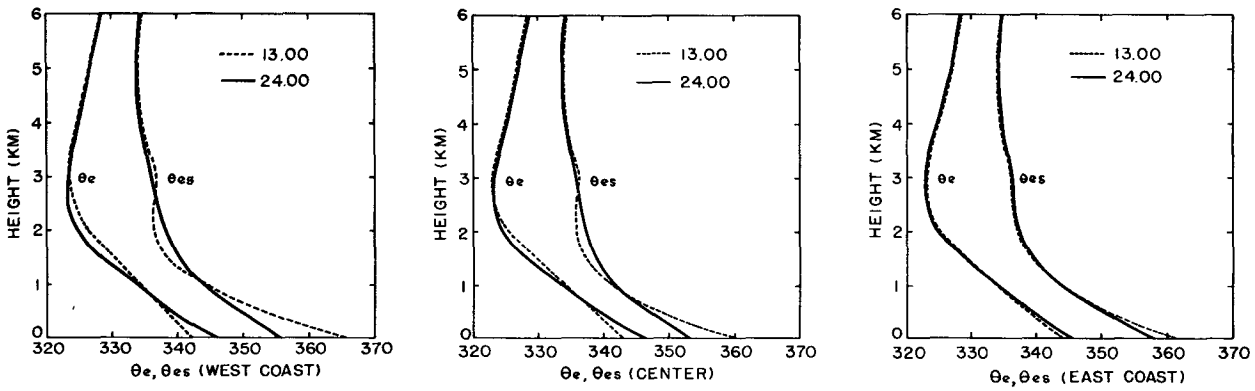

FIG. 19. Vertical profiles of the saturation equivalent potential temperature (θ_{es}) and equivalent potential temperature (θ_e) at 1300 and 2400 LST, for the east coast, center of the island and the west coast.

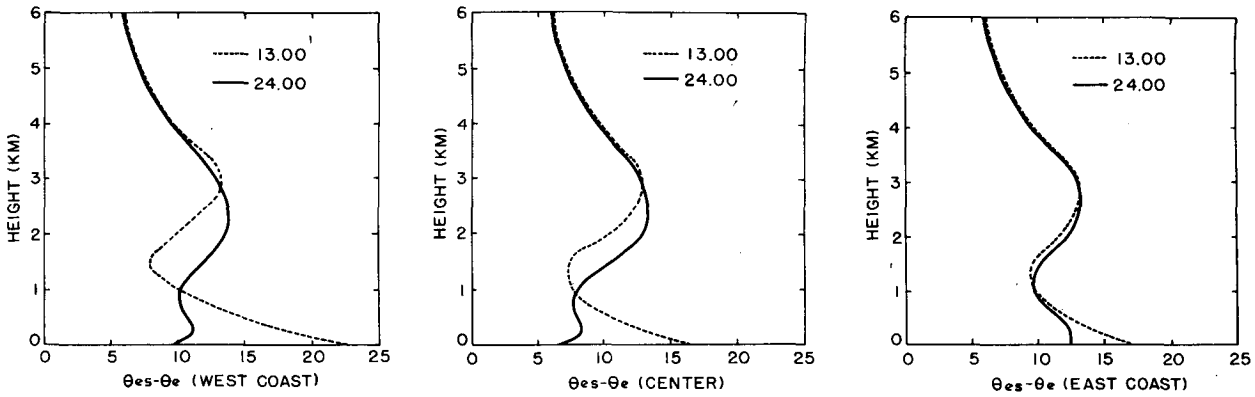

FIG. 20. The difference $(\theta_{es}-\theta_e)$ at 1300 and 2400 LST, for the east coast, center of the island and the west coast.

is, the moister environment below cloud base at night is more conducive to showers, even though the atmosphere above 1 km is drier. This follows because the formation of rain on synoptically undisturbed days is undoubtedly due to warm cloud processes, so that deep cumulus are not required for precipitation. This conclusion is rather speculative and its validity should be examined carefully by observations.

b. Flat island

In this experiment topography is neglected, therefore all differences from the previous experiment can be attributed to terrain effects. Figs. 21 and 22 show the vertical velocity fields along the $j=8\frac{1}{2}$ cross section at 1300 LST and 2400 LST, respectively. At 1300 LST, sinking motion of up to 2 cm s^{-1} is observed at low layers over and off the east coast, while sinking motions as high as 6 cm s^{-1} occur at most upper levels (≥ 2 km) above the island. The nighttime vertical velocity fields (Fig. 22) are very weak with upward motion ≤ 0.5 cm s^{-1} over the eastern part, and downward motion of the same magnitude over the western side of the island. A comparison of Figs. 21 and 22 with Figs. 7 and 8 shows that only in the presence of topography does a low-level region of substantial sinking motion occur over the western part and the center of the island. Lee (1973) obtained the same conclusion in this two-dimensional model. Another feature of the topography is the upward motion over the eastern slopes. This was not mentioned by DeSouza (1972), apparently, because he neglected to consider terrain slope in his convergence calculations. The development of comparatively strong upward motion downwind of the island in this experiment is similar to that simulated for the real island experiment.

c. Two-dimensional forcing experiment

In order to examine the effect of three-dimensional asymmetries, we have carried out an integration equivalent to the first experiment, but for an infinitely long, rectangular island with constant topography in the north–south direction. The width and topography were taken to be that of the $j=8\frac{1}{2}$ grid point of the real island. The boundary condition along the north and south boundaries were changed to $(\partial/\partial y)(w^*,s,u,v)=0$, and the number of grid points in the y direction were reduced to 6.

The vertical velocity field for the steady-state solution is shown in Fig. 23. Comparison with Fig. 5 shows that although the actual values may differ, the spatial distribution is almost identical. The upward vertical velocities on the east coast are slightly larger, with a maximum of 18 cm s^{-1} in contrast to 16 cm s^{-1} in the

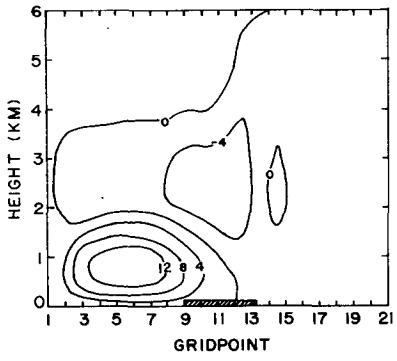

FIG. 21. Vertical velocity field (cm s^{-1}) along the widest east–west cross section at 1300 LST for the flat island experiment.

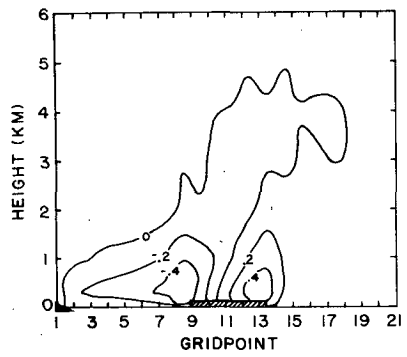

FIG. 22. As in Fig. 21 except for 2400 LST.

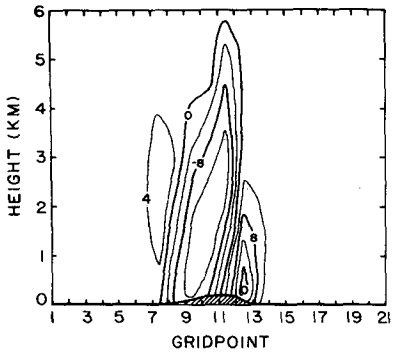

FIG. 23. Vertical velocity field (cm s^{-1}) at 1900 LST for the two-dimensional forcing experiment.

real island simulation case. Maximum rising motion off the west coast at the upper layers are 7 cm s^{-1}, while in the real island case they were 13 cm s^{-1}. Only minor changes in the vertical velocity field are observed at 1300 (Fig. 24) with the upward velocities at the east coast increasing at the 50 and 100 m layers by about 2 cm s^{-1}. Above the center of the island and over the west coast the downward motion has increased by an amount of 1 to 3 cm s^{-1}, in comparison to an increase of sinking by 8 cm s^{-1} above the center in the real island case (Fig. 6).

The most surprising result of our calculation is the *non-appearance* of the large upward velocities downwind from the west coast at low elevation as observed in experiments in Sections 6A and 6B. This must be due to the neglect of the three-dimensional asymmetries of Barbados, which create low-level convergence downstream from the island due to the advection offshore of the positive temperature anomaly. Thus, it is clear from our results that a two-dimensional model of the air flow over Barbados *cannot* give accurate results.

7. Conclusion

We have developed a general three-dimensional model which includes topographic effects to study the influence of a local heat source on the large-scale prevailing flow. An application of the model has been made to examine the air flow over Barbados for three cases—

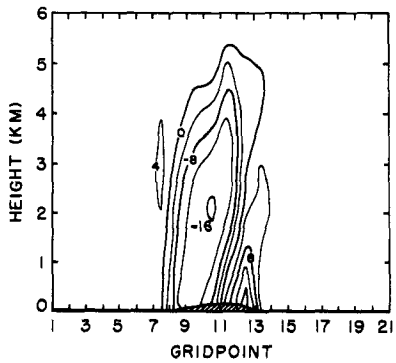

FIG. 24. As in Fig. 23 except for 1300 LST.

1) real island topography, 2) flat island, and 3) infinitely long rectangular island. The temporal variation of the vertical velocity fields described in Section 6a indicate that most of the changes occur at and off the west coast, while at the center of the island and along the east coast only small variations in magnitude are apparent. Thus, the higher frequency of shower activity at night on synoptically undisturbed days cannot be explained in terms of daytime divergence and nighttime convergence over the island. The drying of the lower atmosphere over and off the west coast during the daytime and its cooling and moistening at nighttime could give us an alternative explanation of this phenomenon. It should be noticed that a nighttime maximum in precipitation is also observed over the open tropical ocean (Tyson *et al.*, 1973).

The model results indicate the following major features:

1) Daytime acceleration of the surface winds over the island.
2) A daytime temperature plume downward from the west coast is developed due to advection.
3) Drying of the low layers at and off the west coast during the daytime.
4) Only in the presence of topography does a low-level region of significant sinking motion develop over the west slopes.
5) Topography induces upward motion over the windward side.
6) Upward motion downwind of the west coast is developed only in the three-dimensional version of the model.

The existing observational studies of the air flow over Barbados confirm the salient features obtained in our real island calculations. However, because of the limitations of the observations it is felt additional meteorological measurements over Barbados are needed.

Acknowledgments. The authors wish to thank Carl Aspliden, David Emmitt, Michael Garstang and Joanne Simpson for their comments regarding the meteorology of Barbados. John Walmsley is thanked for pointing out the error in the ψ_2 formulation in Pielke and Mahrer (1975). This work was supported by the National Science Foundation under Grant ATM-74-12559 A01. Acknowledgment is made to the National Center for Atmospheric Research, which is sponsored by the National Science Foundation, for computer time used in this research. Judy Bitting drafted the figures, and Carol Watson and Evelyn Arnette did an excellent job of typing the manuscript. Jeffry Kloss performed the photographic work. Robert Evans did a superb job in recording the original program (Pielke, 1974) onto the NCAR CDC 7600, and his support is gratefully appreciated.

APPENDIX

Partial List of Symbols

f	Coriolis parameter
i, j, k	east–west, north–south and vertical grid index
k_0	von Kármán's constant
$K_z^m, K_z^{\theta_v}, K_z$	vertical exchange coefficient of momentum, heat and moisture
K_H	horizontal exchange coefficient
P_{00}	reference pressure
q	specific humidity
$\bar{s}$	initial height of the material surface
s	material surface top of the model
u, v, w	east–west, north–south and vertical component of velocity
U_g, V_g	east–west and north–south geostrophic wind
U_*	surface friction velocity
w^*	vertical (z^*) component of velocity
x, y, z	Cartesian coordinates
z^*	vertical terrain—following coordinate
z_G	ground elevation
z_0	roughness parameter
z_i	depth of the planetary boundary layer
α	nondimensional numerical constant in the horizontal exchange coefficient ($=0.36$)
π	Exner's function $=c_p(p/P_{00})^{R/c_p}$
θ_v	virtual potential temperature
θ_{v*}	surface friction temperature
θ_{v_s}	surface virtual potential temperature (at level z_0)
$\partial\theta_v^+/\partial z$	virtual potential temperature gradient immediately above the planetary boundary layer
$\Delta x, \Delta y, \Delta z^*$	mesh interval in x, y and z^* components.

REFERENCES

Betts, A. K., 1974: Thermodynamic classification of tropical convective soundings. *Mon. Wea. Rev.*, **102**, 760–764.

Businger, J. A., 1973: Turbulent transfer in the atmospheric surface layer. *Workshop in Micrometeorology*, Amer. Meteor. Soc., Chap. 2.

Clarke, R. H., 1970: Recommended methods for the treatment of the boundary layer in numerical models. *Aust. Meteor. Mag.*, **18**, 51–73.

Deardorff, J., 1974: Three-dimensional numerical study of the height and mean structure of a heated planetary boundary layer. *Boundary-Layer Meteor.*, **7**, 81–106.

Deaven, D. G., 1974: A solution for boundary problems in isentropic coordinate models. Ph.D. dissertation, The Pennsylvania State University, 136 pp.

DeSouza, R. L., 1972: A study of atmospheric flow over a tropical island. Ph.D. dissertation, Florida State University, 203 pp.

Emmitt, D. G., 1975: Momentum redistribution by enhanced mixing over heated islands. Ph.D. dissertation, University of Virginia, 193 pp.

Estoque, M. A., and C. M. Bhumralkar, 1969: Flow over a localized heat source, *Mon. Wea. Rev.*, **97**, 850–859.

Garstang, M., 1967: The role of momentum exchange in flow over a heated island. *Proc. 1967 Army Conf. Tropical Meteorology*, University of Miami, Florida, 178–195.

Holley, R. M., 1972: Surface temperature of a tropical island and surrounding ocean measured with an airborne infrared radiometer. M.S. thesis, The Florida State University, 249 pp.

Hovermale, J. B., 1965: A non-linear treatment of the problem of air flow over mountains. Ph.D. dissertation, The Pennsylvania State University, 86 pp.

Lee, J. D., 1973: Numerical simulation of the planetary boundary layer over Barbados, W. I. Ph. D. dissertation, Florida State University, 101 pp.

Lilly, D. K., and P. J. Kennedy, 1973: Observational of stationary mountain wave and its associated momentum flux and energy dissipation. *J. Atmos. Sci.*, **30**, 1135–1152.

Mahrer, Y., and R. A. Pielke, 1975: A numerical study of the airflow over mountains using the two-dimensional version of the University of Virginia mesoscale model. *J. Atmos. Sci.*, **32**, 2144–2155.

O'Brien, J. J., 1970: A note on the vertical structure of the eddy exchange coefficient in the planetary boundary layer. *J. Atmos. Sci.*, **27**, 1213–1215.

Pielke, R. A., 1974: A three-dimensional numerical model of the sea breezes over soth Florida. *Mon. Wea. Rev.*, **102**, 115–139.

——, and Y. Mahrer, 1975: Technique to represent the heated-planetary boundary layer in mesoscale models with coarse vertical resolution. *J. Atmos. Sci.*, **32**, 2288–2308.

Tyson, P. D., M. Garstang and G. D.Emmitt, 1973: The structure of heat islands. *Rev. Geophys. Space Phys.*, **13**, 139–165.